

A Bioresorbable Magnetically Coupled System for Low-Frequency Wireless Power Transfer

Qinglei Guo, Jahyun Koo, Zhaoqian Xie, Raudel Avila, Xinge Yu, Xin Ning, Hao Zhang, Xu Liang, Sung Bong Kim, Ying Yan, Matthew R. MacEwan, Hyuck Mo Lee, Aimin Song, Zengfeng Di, Yonggang Huang, Yongfeng Mei, and John A. Rogers*

Bioresorbable electronic technologies form the basis for classes of biomedical devices that undergo complete physical and chemical dissolution after a predefined operational period, thereby eliminating the costs and risks associated with secondary surgical extraction. A continuing area of opportunity is in the development of strategies for power supply for these systems, where previous studies demonstrate some utility for biodegradable batteries, radio frequency harvesters, solar cells, and others. This paper introduces a type of bioresorbable system for wireless power transfer, in which a rotating magnet serves as the transmitter and a bioresorbable antenna as the remote receiver, with capabilities for operation at low frequencies (<200 Hz). Systematic experimental and numerical studies demonstrate several unique advantages of this system, most significantly the elimination of impedance matching and electromagnetic radiation exposure presented with the types of radio frequency energy harvesters explored previously. These results add to the portfolio of power supply options in bioresorbable electronic implants.

1. Introduction

Recent advances in unusual electronic materials have led to the development of temporary bioresorbable electronic implants for diagnostic or therapeutic applications,^[1–5] analogous to much simpler passive devices such as resorbable sutures and drug delivery systems. Examples span platforms that utilize both inorganic or organic materials as functional layers, including various types of sensors for tissue and health status monitoring,^[5–9] stimulators for nonpharmacological neuroregenerative therapy,^[10] bioresorbable integrated electronic systems,^[11–13] and many others. Despite recent progress in the electronics and the sensors, many opportunities remain for the development of additional options for power

Prof. Q. L. Guo, Prof. A. M. Song
Center of Nanoelectronics
School of Microelectronics
Shandong University
Jinan 250100, P. R. China

Dr. J. Koo, Dr. S. B. Kim
Simpson Querrey Institute and Feinberg Medical School
Center for Bio-Integrated Electronics
Northwestern University
Evanston, IL 60208, USA

Dr. Z. Q. Xie, Dr. R. Avila, Prof. Y. G. Huang
Department of Civil and Environmental Engineering
Mechanical Engineering, and Materials Science and Engineering
Center for Bio-Integrated Electronics
Northwestern University
Evanston, IL 60208, USA

Prof. X. G. Yu
Department of Biomedical Engineering
City University of Hong Kong
Hong Kong 999077, P. R. China

Prof. X. Ning
Department of Aerospace Engineering
Pennsylvania State University
University Park, PA 16802, USA

Prof. H. Zhang
Department of Chemistry
Key Laboratory of Bioorganic Phosphorus Chemistry & Chemical Biology
Tsinghua University
Beijing 100084, China


Prof. X. Liang
State Key Laboratory for Strength and Vibration of Mechanical Structures
Xi'an Jiaotong University
Xi'an 710049, P. R. China

Dr. Y. Yan, Dr. M. R. MacEwan
Department of Neurological Surgery
Washington University School of Medicine
St Louis, MO 63110, USA

Prof. H. M. Lee
Department of Materials Science and Engineering
Korea Advanced Institute of Science Technology
Daejeon 34141, Republic of Korea

Prof. Z. F. Di
State Key Laboratory of Functional Materials for Informatics
Shanghai Institute of Microsystem and Information Technology
Chinese Academy of Sciences
Shanghai 200050, P. R. China

Prof. Y. F. Mei
Department of Materials Science
Fudan University
Shanghai 200433, P. R. China

 The ORCID identification number(s) for the author(s) of this article can be found under <https://doi.org/10.1002/adfm.201905451>.

DOI: 10.1002/adfm.201905451

supply for these systems. The simplest approach involves fine wires that pass through the skin to connect implanted devices to external hardware. The risks of infection at the skin/wire interface and the constraints that follow from physical tethering represent significant drawbacks. Attractive alternatives include biodegradable batteries,^[14–16] photovoltaic microcells,^[17] supercapacitors,^[18] and triboelectric nanogenerators.^[19] Most of these systems involve, however, one or more disadvantages in limited lifetime, modest power output, and/or only partial degradability.

One of the most versatile choices relies on wireless radio frequency (RF) energy harvesting.^[10,20,21] Recently, Koo et al. reported an Mg-based RF energy harvester,^[10] as the basis of a bioresorbable electrical stimulator for enhanced neuroregeneration. With optimized geometrical designs for the transmitter and receiver, the output voltages can reach tens of volts, capable of providing sufficient electrical power for many classes of implants. However, RF operation requires costly equipment and complex electrical connections. Translational and/or angular misalignments of the transmitting and receiving coils can degrade the transfer efficiency. Important additional considerations in wireless power transfer for such applications include: i) ability for complete bioresorption; ii) low cost, simple designs, iii) reliable, robust performance with motion and/or changes in the ambient environment; iii) negligible absorption of power by biological tissues; and iv) dynamic control over the magnitude of the transferred power.

Here, we demonstrate a wireless magnetic energy harvester based on a rotating permanent magnet that electromagnetically couples to a receiver constructed using entirely biodegradable materials, as an additional option in power supply to temporary implants. Key advantages are in capabilities for operating at low frequencies (<200 Hz) and for operation across a diverse range of scenarios, including several receivers simultaneously, due to the absence of requirements in precise impedance matching. Controlling the rotational frequencies provides a simple scheme for adjusting the transferred power, across levels relevant to powering simple optoelectronic devices (e.g., light emitting diodes, LEDs), radios, or electrical stimulators, of broad utility in not only to implants but also wearable devices, soft robotic systems, and others.

2. Results and Discussion

Figure 1a shows schematic illustrations of the system design and the key constituent materials. The fabrication process flow appears in Figure S1, Supporting Information. Here, the receiver consists of two Mg coils ($\approx 30 \mu\text{m}$ in thickness) connected in a series with a poly (lactic-co-glycolic acid) (PLGA) layer as an

interlayer dielectric. The vertically stacked design increases the number of turns at a fixed horizontal area. The transmitter consists of an electric motor (Zhengke Electromotor Co. Ltd, China), a speed controller, and a neodymium disc magnet (9 mm in diameter, 5 mm in thickness). The diagram in Figure 1b outlines the working principle. The horizontal plane of the receiver coil and the surface of the magnet are oriented in an approximately parallel fashion, and the center of the coil aligns to the center of the magnet. Rotation changes the magnetic flux through the coil at a rate that depends on the rotational frequency, to produce an electromotive force (i.e., voltage) in the receiver, by Faraday's law. Details of the magnetic field distribution and magnetic flux variation appear in finite element analysis (FEA) results highlighted in the top right inset of Figure 1b and in Figure S2 of the Supporting Information. Compared to a coil by a voltage-controlled oscillator, a rotating magnet can generate a much higher magnetic flux at low frequencies, as shown in Figure S3 (Supporting Information).

With the magnet rotating, the induced open-circuit voltage can be determined by connecting the output ends of the receiver to a semiconductor parameter analyzer. As shown in Figure 1c, this voltage exhibits stable and long-term repeatable behavior under different frequencies (f , depended on rotation speeds). Moreover, the required output voltage can be obtained by appropriate selection of the operation frequency, which is defined as the rotation speed of the electrical motor, with a typical range from several to hundreds of Hz. The short-circuit current, as captured in Figure 1d, exhibits a similar response. For a rotation frequency of 51 Hz, the average peak-to-peak voltage (V_{p-p}) is 418 mV, with experimental results (Exp., black dots) that match with simulations (Sim., red line), as shown in Figure 1e. In addition to the rotation rate, the frequency of the output voltage depends on the number of magnets on the coupler. However, V_{p-p} obtained from the magnetic energy harvester with different numbers of magnets does not change significantly for a given rotation rate as demonstrated in Figure S4 of the Supporting Information.

According to Faraday's law, the induced voltage depends on the rate of change of the magnetic flux, such that V_{p-p} and I_{p-p} increase linearly with rotational frequency, as demonstrated in Figure 1f, for a given receiver geometry and working distance (defined as distance between receiver and transmitter). Given that the working area of the harvester is 0.78 cm^2 , the peak output power density (P) at a frequency of 51 Hz is 8.7 mW cm^{-2} . This power density is far higher than that from ZnO-based harvesters (10 nW cm^{-2} ,^[22] $\approx 1 \mu\text{W cm}^{-2}$,^[23] 0.44 mW cm^{-2} ,^[24] depending on many design and application details), biodegradable batteries (0.27 mW cm^{-2} ,^[25] depending on many details), and biodegradable monocrystalline silicon solar cells (1.7 mW cm^{-2} , for illumination with red light through the biological tissues).^[17] The output power density reaches about 10 mW cm^{-2} at a frequency of 58 Hz, as shown in Figure 1g, and its magnitude is proportional to the square of the frequency, consistent with simulation. The power can also be increased by increasing the magnetic field, as shown in Figure S5 of the Supporting Information for the case of two stacked magnets.

Enabling power delivery across sufficiently long working distances is crucial for use in implants. At a minimum, the working distance should be larger than the mean skin

Prof. J. A. Rogers
Departments of Materials Science and Engineering
Biomedical Engineering, Neurological Surgery, Chemistry
Mechanical Engineering
Electrical Engineering and Computer Science
Center for Bio-Integrated Electronics
Northwestern University
Evanston, IL 60208, USA
E-mail: jrogers@northwestern.edu

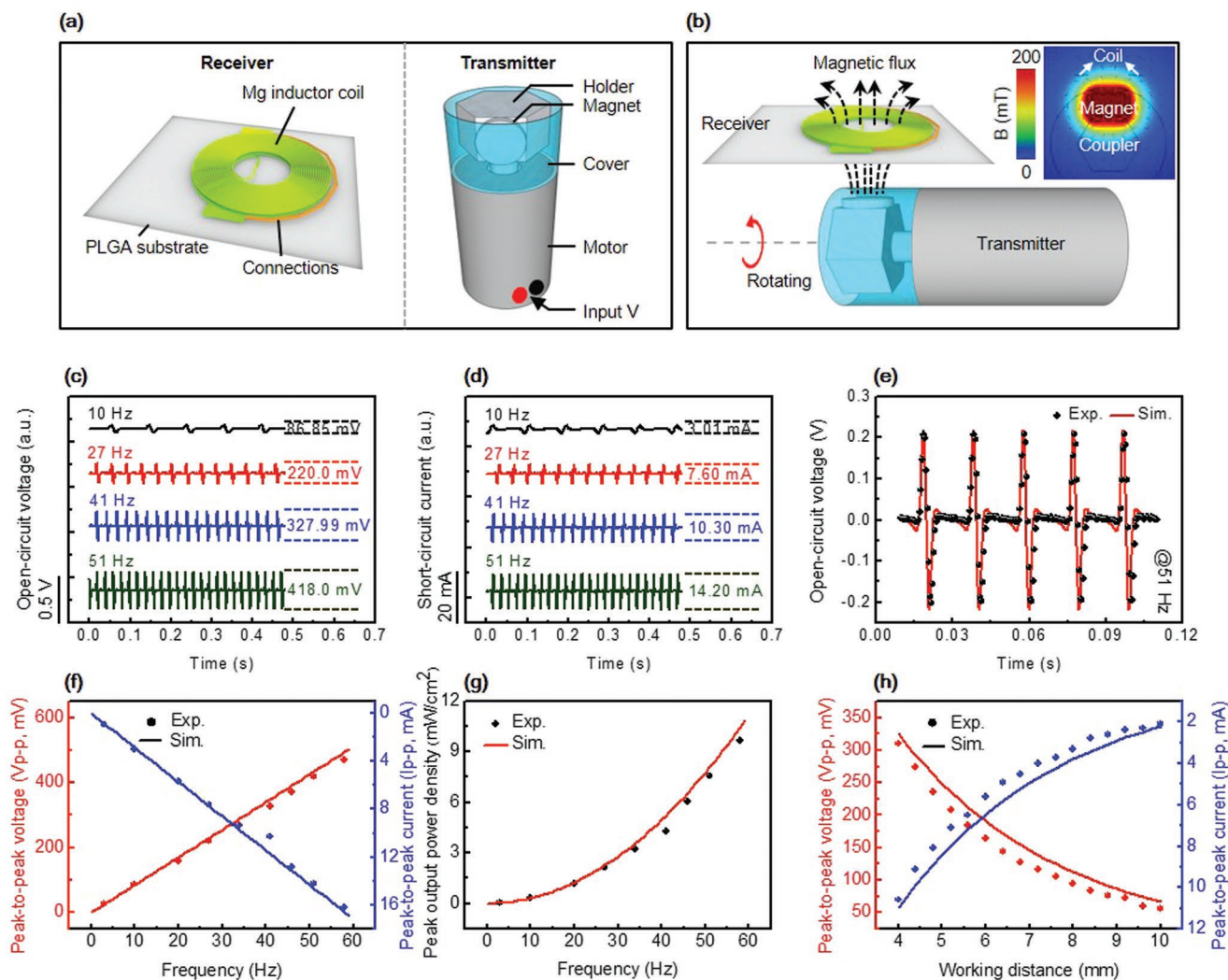


Figure 1. a) Schematic illustrations of an Mg coil as the receiver on a PLGA substrate and a rotating magnet as a transmitter for wireless power transfer. b) Schematic diagram of the working principles. The simulated magnetic field intensity distribution appears in the top-left. c,d) Open-circuit voltages and short-circuit currents delivered to the receiver at several rotational frequencies (i.e., 10, 27, 41, and 51 Hz) of the transmitter. e) Experimental (black dots) and simulated (red line) results for open-circuit voltages at a frequency of 51 Hz. f) Simulations and experimental results for open-circuit voltages (red dots: exp., red line: sim.) and short-circuit currents (blue dots: exp., blue line: sim.) at different frequencies. g) Simulations (red line) and experimental results (red dots) for peak output power densities at various frequencies. The distance between the receiver and transmitter for (c–g) is 4 mm. h) Simulations and experimental results for peak-to-peak voltages (red dots: exp., red line: sim.) and currents (blue dots: exp., blue line: sim.) for different working distances at a frequency of 38.5 Hz.

thickness, typically between 1.5 and 2.5 mm.^[26] Measurements and simulations of open-circuit voltage and short-circuit current at a fixed frequency (38.5 Hz) appear in Figure 1h as a function of distance. Voltages larger than 300 mV can be achieved at a distance of 4 mm. As this distance increases, both V_{p-p} and I_{p-p} decrease in an approximately exponential manner, consistent with the reduction in field with distance (see Figure S6, Supporting Information). The decrease of V_{p-p} with distance can be compensated, to some extent, by increasing the frequency.

Figure 2 demonstrates the wide applicability of this approach through demonstrations that involve three coils with different geometries, as schematically displayed in Figure S7 in the Supporting Information, and different associated RF resonances, as in Figure 2a (Coil 1–35 MHz; Coil 2–23 MHz; and

Coil 3–19 MHz). Despite the differences, effective open-circuit voltages can be induced in all cases, as shown in Figure 2b, with expected linear relationships between V_{p-p} and frequency (Figure 2c). The simulations, which account for geometrical differences, show excellent agreement with experiment.

Schematic illustrations of experiments to explore the effects of the environment and, in particular, the influence of materials with different dielectric properties between the transmitter and receiver appear in Figure 2d. Examples include air, a plastic container, deionized water (DIW), phosphate buffered saline (PBS, pH = 7.0), poly(dimethylsiloxane) (PDMS), bioresorbable wax, and raw chicken meat, as in Figure S8 (Supporting Information). Pictures for air and chicken are in Figure S9 (Supporting Information). The experiments use a frequency 40 Hz,

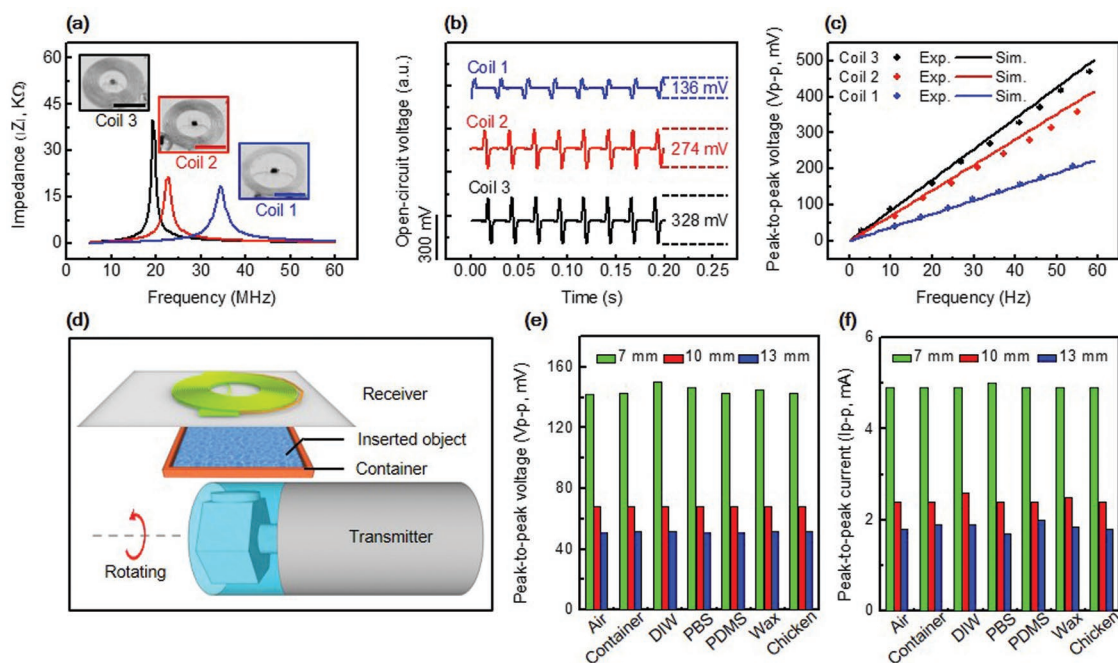


Figure 2. a) Graph of impedance as a function of frequency for three different coils (Coil 1, Coil 2, and Coil 3), each with a different resonant frequency. Images of these coils appear in the inset. b) Open-circuit voltages delivered by wireless power transfer to these coils, for a fixed working distance and frequency of 4 mm and 41 Hz, respectively. c) Simulations (lines) and experimental results (dots) for peak-to-peak output voltages generated from Coil 1, Coil 2, and Coil 3, at a working distance of 4 mm. d) Schematic diagram of the system with an object inserted between the receiver and transmitter. e, f) Peak-to-peak values of output voltage and current collected from a typical coil (here, Coil 3) for cases of various objects, including a plastic container, deionized water (DIW), phosphate buffer (PBS, pH = 7.0), poly(dimethylsiloxane) (PDMS), bioresorbable wax, and raw chicken meat, for working distances of 7, 10, and 13 mm, respectively. The case without any inserted object is labeled as “Air.” The frequency is 40 Hz for all examples.

at three working distances (i.e., 7, 10, 13 mm). As shown in Figure 2e,f, both V_{p-p} and I_{p-p} are similar for all cases examined, as expected.

A magnetic field concentrator (MFC) formed from a composite of biodegradable iron oxide nanoparticles^[27] (Fe_2O_3 , ≈ 50 nm in diameter) and PLGA, placed on top of the receiver coils can enhance the performance. The magnetic hysteresis loop of the MFC is in Figure S10 (Supporting Information), consistent with its ferromagnetic behavior. As shown in Figure 3a,b, a receiver structure that consists of MFC cover/Mg coil/PLGA interlayer/Mg coil/PLGA substrate can be compared to one that replaces the MFC cover with a layer of PLGA, both operated at a frequency and a working distance of 43.45 Hz and 4 mm, respectively. Figure 3c shows a $\approx 14\%$ enhancement in V_{p-p} associated with the structure that uses the MFC, at various frequencies, as shown in Figure 3d. Furthermore, as the working distance increases, the magnetic field concentration effect of MFC persists, as demonstrated in Figure 3e through an enhanced V_{p-p} for a working distance from 4 to 10 mm.

Robust performance demands some tolerance to misalignment, defined by the distance between the projection of the center of the receiver and the center of the transmitter along the horizontal direction, as schematically illustrated in Figure S11 (Supporting Information). The influence of misalignment can be compared through measurements of V_{p-p} for receivers with and without an MFC, at a frequency and working distance of 43.45 Hz and 4 mm, respectively. As presented in Figure 3f,

V_{p-p} obtained from the receiver without MFC (Exp., black dots; Sim., black line) decreases with small misalignments (< 3 mm) and then drastically diminishes as the misalignment increases to 10 mm. By contrast, V_{p-p} obtained using a receiver with an MFC at a misalignment of 6 mm is comparable with that from a receiver without MFC at zero misalignment, as demonstrated in Figure 3f with a dashed orange line. Appropriate choices of magnetic materials for MFC offer the potential to further reduce the effects of misalignment.

Previous studies demonstrate that iron oxide nanoparticles can be intracellularly degraded in the body,^[28] and recycled by iron metabolism,^[29] thus yielding biocompatible and biodegradable behaviors. In vitro studies based on immersion in PBS at pH = 7 and 50 °C) yield data on accelerated aging. Scanning electron microscope (SEM) imaging at various times reveals changes in the micro/nanostructure as shown in Figure 3g. The degradation of the MFC starts with the PLGA by hydrolysis of its ester linkages.^[30] As PBS penetrates the interface between iron oxide nanoparticles and PLGA, voids form and grow due to the release of iron oxide nanoparticles. A set of images collected from a receiver with an MFC at various times of immersion in PBS (pH = 7, 37 °C) is in Figure 3h. The dissolution process triggers disintegration, as each constituent material (Mg, PLGA, and iron oxide nanoparticles) disappears at different rates.^[10,28,31] Functional degradation of the open-circuit voltage collected from double-layered coils encapsulated in PLGA and immersed DI water at

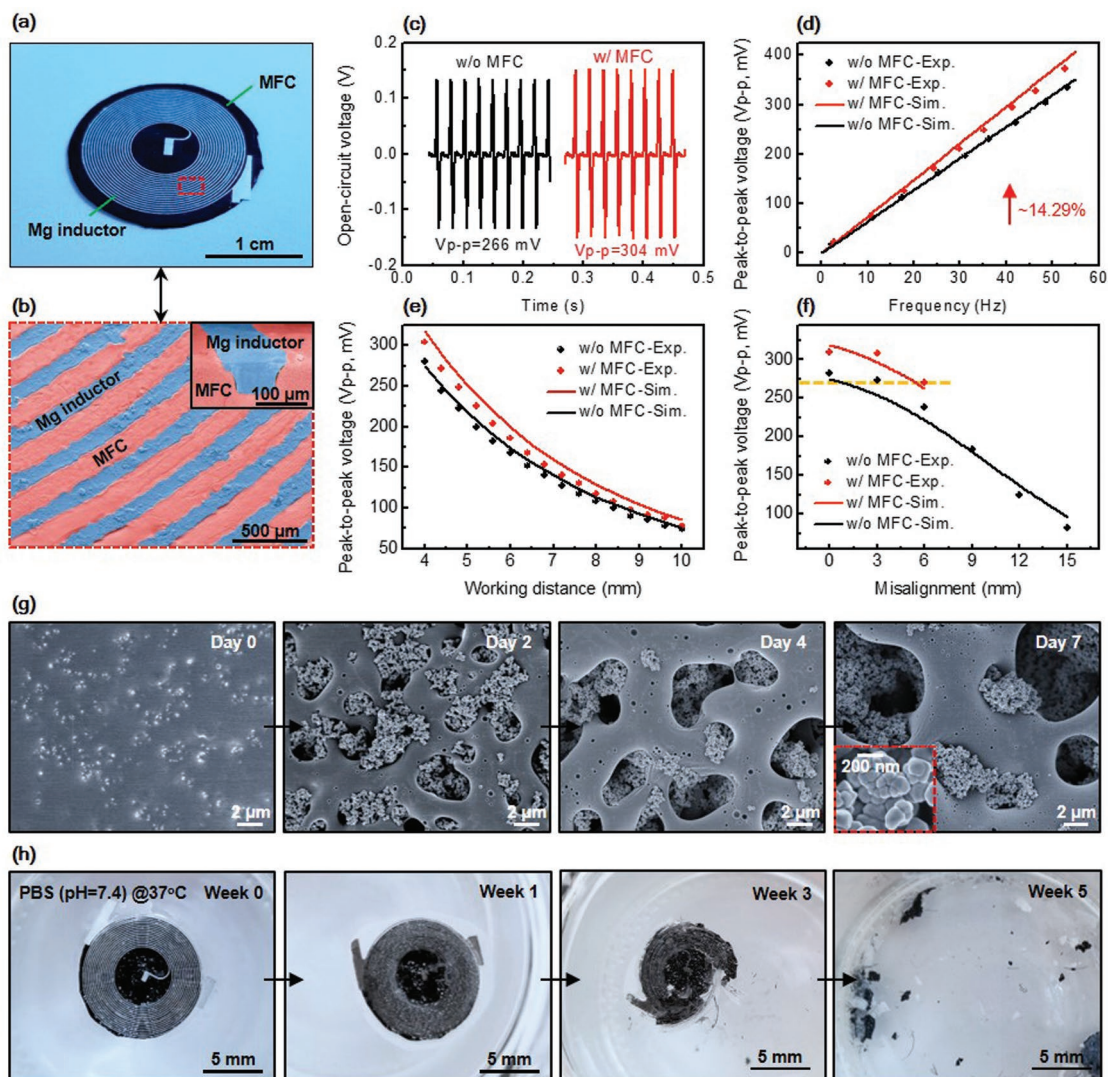


Figure 3. a) Optical image of an Mg coil after integration with a magnetic flux concentrator (MFC). b) Colorized SEM images (main: plane view; inset: cross-section view) of a coil transferred on an MFC. c) Open-circuit output voltages from an Mg coil without (w/o) and with (w/) an MFC. The frequency and working distance for the system is 43.45 Hz and 4 mm, respectively. d) Simulations (lines) and experimental results (dots) for the peak-to-peak voltages for Mg coils with (red) and without (black) an MFC, measured at various frequencies and a working distance of 4 mm. The MFC yields an average enhancement of 14%. e) Simulations and experimental results for the peak-to-peak voltage at various working distances for an Mg coil with and without an MFC, at a frequency of 43.45 Hz. f) Simulations and experimental results for the peak-to-peak voltage under various misalignment conditions for Mg coil with and without an MFC, at a frequency of 43.45 Hz and working distance of 4 mm. The misalignment corresponds to the horizontal distance between the centers of the receiver coil and transmitter. g) SEM images of the dissolution of an MFC due to immersion in phosphate buffer solution (PBS, pH 7, at 50 °C). h) Optical images of the dissolution of a bioresorbable receiver with an MFC.

37 °C as a function of time over a period of 10 h (Figure S12, Supporting Information). Designs that offer reduced rates of dissolution may decrease/eliminate risks for toxicity. The timescales for dissolution can be controlled by appropriate choices of materials (other biodegradable metals or polymers) and by geometrical parameters (such as thickness, dimension, and configuration). Utilizing alternative encapsulation materials, such as thermal oxide,^[7] can also provide extended timescales for dissolution. On-going work focuses on developing additional materials options.

Figure 4 summarizes examples of the use of these power supplies. In the first, operation of a LED follows from power

supplied by a receiver with five coils vertically stacked and connected in series (see the photograph in Figure S13 in the Supporting Information), as shown in Figure 4a. The top right inset of Figure 4a provides an optical image of the LED, and the bottom right inset shows a schematic diagram of the equivalent circuit. Figure 4b displays waveforms associated with open-circuit voltages collected from this receiver, operated with a transmitter at a frequency of 83 Hz and a working distance of 4 mm. The peak-to-peak voltage can reach ≈ 3.26 V, with a capability for further enhancement with an MFC, as demonstrated in Figure S14 (Supporting Information). This voltage is sufficient to operate the LED (Figure 4c).

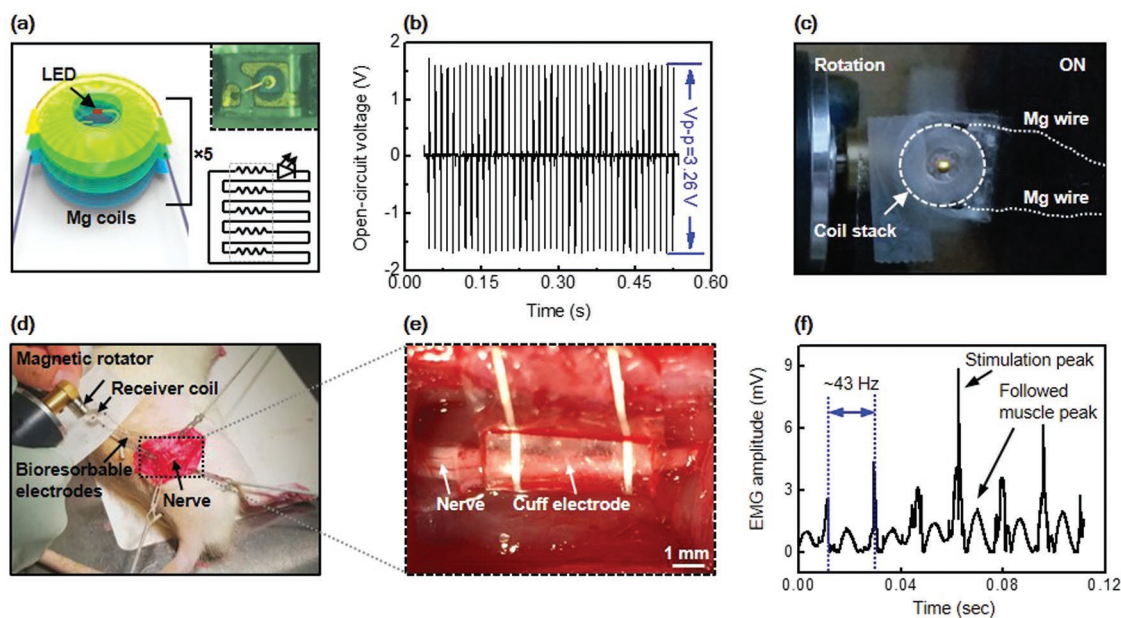


Figure 4. Demonstration of a wireless power transfer system designed to operate an LED. a) Schematic diagram of five Mg coils in a vertical stack. The bottom-right shows an equivalent circuit. An optical microscope image of the LED appears in the top-right. b) Open-circuit voltage collected from the system, showing peak-to-peak voltage (V_{p-p}) of 3.26 V, sufficient to operate the LED, for a frequency and working distance of 83 Hz and 4 mm, respectively. c) Image of the system during operation of the LED. d) Optical image of the system as a wireless, bioresorbable stimulator for the sciatic nerve in a rat model. e) Magnified optical image of the bioresorbable cuff electrode conformally wrapped around the sciatic nerve. f) The effective muscle activation was captured using Red Rock Laboratories acquisition software (version 2.0) during the stimulation. The measured stimulated period is about 43 Hz, consistent with the rotation frequency, as expected.

Figure 4d shows a different example, in which wireless power passes an Mg cuff electrode interfaced to the right side of sciatic nerve in a Lewis rat model. A laser-cut pattern of Mg serves as electrodes transfer-printed onto a PLGA substrate to enable conformal contact with the nerve for electrical stimulation, as shown Figure 4e. The Mg cuff electrode electrically connects to the Mg receiver with a bioresorbable conductive paste.^[32] Figure 4f shows the muscle response obtained from the tibialis anterior muscle in uninjured animals using electromyography (EMG) measurement (Red Rock Laboratories, Version 2.0, St. Louis, MO), during stimulation.^[10] Slight changes in position of the hand-held magnetic rotator result in variations in the amplitudes of the peaks associated with the stimulation. The EMG peaks lie above the threshold (≈ 3 mV) for muscle activation, with a periodic behavior at a frequency of ≈ 43 Hz, identical to that of the transmitter. These values, as reported previously,^[10] correspond to stimulation of all of the nerve fibers via the electrodes placed around the target sciatic nerve (more details can be found in Movie S1 of the Supporting Information).

3. Conclusion

In summary, the results presented here provide the basis for a simple and convenient approach to wireless power supply in biodegradable electronics. The low-frequency operation and ability to deliver practical amounts of power for realistic biomedical applications, for example, as power supplies for temporary implantable sensors and nerve stimulators, in

platforms that are built entirely with biocompatible and bioresorbable materials represent the main points of interest. Systematic studies including experiments and simulations reveal all of the key design considerations. The biodegradable magnetic field concentrator is an important component, of likely additional utility in other applications that demand magnetic functionality. The presented demonstrations foreshadow opportunities in optical and/or electrical stimulation, as potential treatment strategies for preventing or curing muscle atrophy, modulating pain responses, accelerating neuron regeneration, and many other related unusual bioelectronic therapies.

4. Experimental Section

Construction of Magnetic Energy Harvester: Fabrication began with the Mg inductor coil. A piece of Mg foil (30 μm , Solution Materials, LLC, USA) attached with a slab of poly(dimethylsiloxane) (PDMS, 9:1) allowed for photolithographic patterning and wet etching (diluted hydrochloric acid, HCl:water = 1:9) to define a single layer coil structure. The Mg coil soaked with a drop of ethyl acetate (Sigma-Aldrich) for 1 min was transferred onto a preformed PLGA (30 μm thick, 65:35 (lactide:glycolide), Sigma-Aldrich) substrate. Placing two such Mg coil/PLGA pieces together, face to face, with a thin preformed PLGA dielectric interlayer and opening for interconnections, completed the fabrication of the bioresorbable Mg inductor coil. A schematic illustration of the fabrication process can be found in Figure S1 of the Supporting Information. Integrating a disc magnet (neodymium, 9 mm in diameter and 5 mm in thickness) with an electric motor (Zhengke Electromotor Co. Ltd, China) using a cooper mounting fixture formed the transmitter. This simple system provided means for generating an alternating

magnetic field with a frequency determined by a speed controller. A triaxial displacement stage allowed precise adjustment of the working distance and alignment between the transmitter and receiver.

Integration of Mg Receivers with a Magnetic Flux Concentrator: The MFC consisted of iron oxide nanoparticles embedded in PLGA. Iron oxide nanoparticles (<50 nm, Sigma-Aldrich) were successively cleaned in acetone, ethanol, and deionized water using an ultrasonic cleaner for 5 min, then dispersed in a mixture of PLGA (65:35 (lactide:glycolide), Sigma-Aldrich) and chloroform. Drop-casting the magnetic dispersion on a silicon substrate formed the MFC after natural evaporation of the solvent at room temperature. A single layer Mg coil on a PDMS temporary substrate was transferred onto the MFC. An additional Mg coil on PLGA placed together with the Mg coil on the MFC, face to face, with a thin PLGA dielectric interlayer and opening for interconnections, formed the bioresorbable, MFC enhanced Mg receiver.

Dissolution Testing: The tests of Mg coils with an MFC involved immersion in PBS (pH 7.4) in a plastic container, where a programmable hotplate maintained the temperature at 37 °C. Dissolution tests of the MFC involved soaking in PBS (pH 7.4; Sigma-Aldrich) in a plastic container, where an oven maintained a set temperature of 50 °C. Ex situ characterization of MFCs designed with different dissolution periods relied on a SEM system (Hitachi S4800). A digital camera captured images of the receiver at different times after immersion in PBS.

Finite Element Analysis: FEA used the commercial software COMSOL 5.2a (Rotating Machinery and Electrical Circuit User's Guide). The rotating machinery, magnetic and electrical circuit modules were used to study the open-circuit voltage/short-circuit for different rotation frequencies (10, 27, 30, 41 Hz). The magnet and coils were modeled using 4-node tetrahedral elements. The area around the coil and MFC had a minimum mesh size of (10 μm), with at least four elements for the thickness direction; the convergence of the simulation was ensured. The air boundary between the rotational domain and the coil had a minimum mesh size of (30 μm) with six layers of elements on each side of the rotational boundary. The area of the magnet had a minimum mesh size of (50 μm). The convergence of the simulation was ensured for all cases. The relative permittivity, electrical conductivity, and relative permeability used in the simulation were 1, 0 S m⁻¹, 1 for air and soft iron; 1, 5.99e7 S m⁻¹, 1 for copper; and 1, 0 S m⁻¹, 20 for the MFC, respectively. The magnet was defined using a magnetization of 670 000 A m⁻¹ in the normal direction and the electrical conductivity and relative permittivity were kept as unity. The external electrical circuit (an external inductor-in-circuit feature) was included to get the open-circuit voltage/short-circuit current of the coils.

Electromagnetic Simulation: The finite element method was used to study the magnetic field around a Cu coil powered by a voltage-controlled oscillator (Figure S3, Supporting information). The simulations were performed using the commercial software Ansys HFSS (Ansys HFSS 15, Ansys Inc. 2012), where the lumped port was used. An adaptive mesh (tetrahedron elements) together with a spherical surface (500 mm in radius) as the radiation boundary, were adopted to ensure computational accuracy. The electromagnetic parameters of Cu in the material library of Ansys HFSS were used in the simulation. The parameters associated with the magnet (diameter, 9 mm; and magnetic field, 116.3 mT) were the same as those used in the experiments.

Evaluation of the Electric Output Properties: The open-circuit voltage and current values were measured by connecting the two ends of the receiver directly to the high-impedance probes of a semiconductor parameter analyzer (4155C; Agilent). Five coils vertically stacked and interconnected with a bioresorbable Mg wire via composites of Mo particles and a biodegradable wax^[32] yielded voltages necessary to power an LED. Increasing the number of turns of the coil could be facilitated by use of pattern techniques that offer resolution higher than those reported here. An LED was placed at the center of the receiver and used an electric connection with the receiver by bioresorbable pastes. Two ends of the receiver coil series were electrically connected using Mg wire to form a closed circuit. Photographs of the operating LED were captured by a digital camera at a dark condition.

Evaluation in an Animal Model: Adult male Lewis rats (275–300 g, aged 10–11 weeks) were anesthetized to allow surgical exposure of the right sciatic nerve. Laser-cut Mg electrodes on flexible PLGA substrates were implanted on the right sciatic nerve and electrically connected to the Mg coils. The Mg coils harvested energy from the hand-held magnetic rotator and delivered a periodic stimulating signal to the right sciatic nerve. Evoked EMG responses were collected using Red Rock Laboratories Data Acquisition Software (Red Rock Laboratories, Version 2.0, St. Louis, MO) and analyzed using MATLAB software (MathWorks, Version 2009B, Natick, MA). All animal procedures were performed in strict accordance with the Animal Studies Committee and the Division of Comparative Medicine at Washington University School of Medicine.

Supporting Information

Supporting Information is available from the Wiley Online Library or from the author.

Acknowledgements

Q.L.G., J.K., and Z.Q.X. contributed equally to this work. Q.L.G. and Z.Q.X. acknowledge the support from the National Natural Science Foundation of China (Grant Nos. 51602056 and 11402134). R.A. acknowledges the support from the Ford Foundation Pre-Doctoral Fellowship and the National Science Foundation Graduate Research Fellowship Program (Grant No. 1842165). Y.G.H. acknowledges the support from NSF (No. CMMI1635443). This work was supported by the Center for Bio-Integrated Electronics at Northwestern University. The author name Xing Ning was corrected to Xin Ning on November 14, 2019 after initial publication online.

Conflict of Interest

The authors declare no conflict of interest.

Keywords

bioelectronics, energy harvesters, RF inductors, transient electronics, wireless power transfer

Received: July 6, 2019

Revised: August 17, 2019

Published online: September 6, 2019

- [1] S.-W. Hwang, H. Tao, D.-H. Kim, H. Cheng, J.-K. Song, E. Rill, M. A. Brenckle, B. Panilaitis, S. M. Won, Y.-S. Kim, Y. M. Song, K. J. Yu, A. Ameen, R. Li, Y. Su, M. Yang, D. L. Kaplan, M. R. Zakin, M. J. Slepian, Y. Huang, F. G. Omenetto, J. A. Rogers, *Science* **2012**, 337, 1640.
- [2] C. M. Boutry, A. Nguyen, Q. O. Lawal, A. Chortos, S. Rondeau-Gagne, Z. Bao, *Adv. Mater.* **2015**, 27, 6954.
- [3] Q. Guo, Z. Di, M. G. Lagally, Y. Mei, *Mater. Sci. Eng., R* **2018**, 128, 1.
- [4] S. K. Kang, J. Koo, Y. K. Lee, J. A. Rogers, *Acc. Chem. Res.* **2018**, 51, 988.
- [5] J. K. Chang, H. P. Chang, Q. Guo, J. Koo, C. I. Wu, J. A. Rogers, *Adv. Mater.* **2018**, 30, 1704955.
- [6] S. K. Kang, R. K. Murphy, S. W. Hwang, S. M. Lee, D. V. Harburg, N. A. Krueger, J. Shin, P. Gamble, H. Cheng, S. Yu, Z. Liu, J. G. McCall, M. Stephen, H. Ying, J. Kim, G. Park, R. C. Webb, C. H. Lee, S. Chung, D. S. Wie, A. D. Gujar, B. Vemulapalli,

- A. H. Kim, K. M. Lee, J. Cheng, Y. Huang, S. H. Lee, P. V. Braun, W. Z. Ray, J. A. Rogers, *Nature* **2016**, 530, 71.
- [7] J. Shin, Y. Yan, W. Bai, Y. Xue, P. Gamble, L. Tian, I. Kandela, C. R. Haney, W. Spees, Y. Lee, M. Choi, J. Ko, H. Ryu, J.-K. Chang, M. Pezhouh, S.-K. Kang, S. M. Won, K. J. Yu, J. Zhao, Y. K. Lee, M. R. MacEwan, S.-K. Song, Y. Huang, W. Z. Ray, J. A. Rogers, *Nat. Biomed. Eng.* **2019**, 3, 37.
- [8] C. M. Boutry, Z. Wang, J. Chang, Y. Kaizawa, B. C. Schroeder, P. Fox, Z. Bao, *Nat. Electron.* **2018**, 1, 314.
- [9] M. S. Mannoor, H. Tao, J. D. Clayton, A. Sengupta, D. L. Kaplan, R. R. Naik, N. Verma, F. G. Omenetto, M. C. McAlpine, *Nat. Commun.* **2012**, 3, 763.
- [10] J. Koo, M. R. MacEwan, S. K. Kang, S. M. Won, M. Stephen, P. Gamble, Z. Xie, Y. Yan, Y. Y. Chen, J. Shin, N. Birenbaum, S. Chung, S. B. Kim, J. Khalifeh, D. V. Harburg, K. Bean, M. Paskett, J. Kim, Z. S. Zohny, S. M. Lee, R. Zhang, K. Luo, B. Ji, A. Banks, H. M. Lee, Y. Huang, W. Z. Ray, J. A. Rogers, *Nat. Med.* **2018**, 24, 1830.
- [11] K. J. Yu, D. Kuzum, S. W. Hwang, B. H. Kim, H. Juul, N. H. Kim, S. M. Won, K. Chiang, M. Trumpis, A. G. Richardson, H. Cheng, H. Fang, M. Thomson, H. Bink, D. Talos, K. J. Seo, H. N. Lee, S. K. Kang, J. H. Kim, J. Y. Lee, Y. Huang, F. E. Jensen, M. A. Dichter, T. H. Lucas, J. Viventi, B. Litt, J. A. Rogers, *Nat. Mater.* **2016**, 15, 782.
- [12] D. Son, J. Lee, D. J. Lee, R. Ghaffari, S. Yun, S. J. Kim, J. E. Lee, H. R. Cho, S. Yoon, S. Yang, S. Lee, S. Qiao, D. Ling, S. Shin, J.-K. Song, J. Kim, T. Kim, H. Lee, J. Kim, M. Soh, N. Lee, C. S. Hwang, S. Nam, N. Lu, T. Hyeon, S. H. Choi, D.-H. Kim, *ACS Nano* **2015**, 9, 5937.
- [13] T. Lei, M. Guan, J. Liu, H.-C. Lin, R. Pfattner, L. Shaw, A. F. McGuire, T.-C. Huang, L. Shao, K.-T. Cheng, J. B.-H. Tok, Z. Bao, *Proc. Natl. Acad. Sci. USA* **2017**, 114, 5107.
- [14] L. Yin, X. Huang, H. Xu, Y. Zhang, J. Lam, J. Cheng, J. A. Rogers, *Adv. Mater.* **2014**, 26, 3879.
- [15] Z. Wang, K. K. Fu, Z. Liu, Y. Yao, J. Dai, Y. Wang, B. Liu, L. Hu, *Adv. Funct. Mater.* **2017**, 27, 1605724.
- [16] K. K. Fu, Z. Wang, C. Yan, Z. Liu, Y. Yao, J. Dai, E. Hitz, Y. Wang, W. Luo, Y. Chen, M. Kim, L. Hu, *Adv. Energy Mater.* **2016**, 6, 1502496.
- [17] L. Lu, Z. Yang, K. Meacham, C. Cvetkovic, E. A. Corbin, A. Vázquez-Guardado, M. Xue, L. Yin, J. Boroumand, G. Pakeltis, T. Sang, K. J. Yu, D. Chanda, R. Bashir, R. W. Gereau, X. Sheng, J. A. Rogers, *Adv. Energy Mater.* **2018**, 8, 1703035.
- [18] G. Lee, S.-K. Kang, S. M. Won, P. Gutruf, Y. R. Jeong, J. Koo, S.-S. Lee, J. A. Rogers, J. S. Ha, *Adv. Energy Mater.* **2017**, 7, 1700157.
- [19] W. Jiang, H. Li, Z. Liu, Z. Li, J. Tian, B. Shi, Y. Zou, H. Ouyang, C. Zhao, L. Zhao, R. Sun, H. Zheng, Y. Fan, Z. L. Wang, Z. Li, *Adv. Mater.* **2018**, 30, 1801895.
- [20] R. H. Kim, H. Tao, T. I. Kim, Y. Zhang, S. Kim, B. Panilaitis, M. Yang, D. H. Kim, Y. H. Jung, B. H. Kim, Y. Li, Y. Huang, F. G. Omenetto, J. A. Rogers, *Small* **2012**, 8, 2812.
- [21] S. W. Hwang, X. Huang, J. H. Seo, J. K. Song, S. Kim, S. Hage-Ali, H. J. Chung, H. Tao, F. G. Omenetto, Z. Ma, J. A. Rogers, *Adv. Mater.* **2013**, 25, 3526.
- [22] C. Dagdeviren, S. W. Hwang, Y. Su, S. Kim, H. Cheng, O. Gur, R. Haney, F. G. Omenetto, Y. Huang, J. A. Rogers, *Small* **2013**, 9, 3398.
- [23] C. Dagdeviren, B. D. Yang, Y. Su, P. L. Tran, P. Joe, E. Anderson, J. Xia, V. Doraiswamy, B. Dehdashti, X. Feng, B. Lu, R. Poston, Z. Khalpey, R. Ghaffari, Y. Huang, M. J. Slepian, J. A. Rogers, *Proc. Natl. Acad. Sci. USA* **2014**, 111, 1927.
- [24] G. Zhu, R. Yang, S. Wang, Z. L. Wang, *Nano Lett.* **2010**, 10, 3151.
- [25] X. Huang, D. Wang, Z. Yuan, W. Xie, Y. Wu, R. Li, Y. Zhao, D. Luo, L. Cen, B. Chen, H. Wu, H. Xu, X. Sheng, M. Zhang, L. Zhao, L. Yin, *Small* **2018**, 14, 1800994.
- [26] A. Laurent, F. Mistretta, D. Bottiglioli, K. Dahel, C. Goujon, J. F. Nicolas, A. Hennino, P. E. Laurent, *Vaccine* **2007**, 25, 6423.
- [27] K. H. Bae, M. Park, M. J. Do, N. Lee, J. H. Ryu, G. W. Kim, C. Kim, T. G. Park, T. Hyeon, *ACS Nano* **2012**, 6, 5266.
- [28] B. Freund, U. I. Tromsdorf, O. T. Bruns, M. Heine, A. Giemsa, A. Bartelt, S. C. Salmen, N. Raabe, J. Heeren, H. Itrich, R. Reimer, H. Hohenberg, U. Schumacher, H. Weller, P. Nielsen, *ACS Nano* **2012**, 6, 7318.
- [29] J. Volatron, F. Carn, J. Kolosnjaj-Tabi, Y. Javed, Q. L. Vuong, Y. Gossuin, C. Menager, N. Luciani, G. Charron, M. Hemadi, D. Alloyeau, F. Gazeau, *Small* **2017**, 13, 1602030.
- [30] S. W. Hwang, J. K. Song, X. Huang, H. Cheng, S. K. Kang, B. H. Kim, J. H. Kim, S. Yu, Y. Huang, J. A. Rogers, *Adv. Mater.* **2014**, 26, 3905.
- [31] L. Yin, H. Cheng, S. Mao, R. Haasch, Y. Liu, X. Xie, S.-W. Hwang, H. Jain, S.-K. Kang, Y. Su, R. Li, Y. Huang, J. A. Rogers, *Adv. Funct. Mater.* **2014**, 24, 645.
- [32] S. M. Won, J. Koo, K. E. Crawford, A. D. Mickle, Y. Xue, S. Min, L. A. McIlvried, Y. Yan, S. B. Kim, S. M. Lee, B. H. Kim, H. Jang, M. R. MacEwan, Y. Huang, R. W. Gereau, J. A. Rogers, *Adv. Funct. Mater.* **2018**, 28, 1801819.